

Comparative Study of the Rytov and Born Approximations in Quantitative Microwave Holography

Daniel Tajik^{*}, Aaron D. Pitcher, and Natalia K. Nikolova

Abstract—Quantitative microwave holography is a recent imaging methodology that shows promise in medical diagnostics. It is a real-time direct inversion algorithm that reconstructs the complex permittivity from S -parameter measurements on an acquisition surface outside of the imaged object. It is recognized that this imaging method suffers from limitations in tissue imaging due to a forward model which linearizes a highly nonlinear scattering problem. It is therefore important to study its limitations when reconstruction is aided by certain pre- and post-processing filters which are known to improve the image quality. The impact of filtering on the quantitative result is particularly important. In this work, the reconstruction equations of quantitative microwave holography are derived from first principles. The implementation of two linearizations strategies, Born's approximation and Rytov's approximation, is explained in detail in the case of a scattering model formulated in terms of S -parameters. Furthermore, real-space and Fourier-space filters are developed to achieve the best performance for the given linearized model of scattering. Simulated and experimental results demonstrate the limitations of the method and the necessity of filtering. The two approximations are also compared in experimental tissue reconstructions.

1. INTRODUCTION

Microwave imaging is an effective strategy for examining optically obscured objects. Current commercial applications include concealed weapons detection, non-destructive testing, and through-the-wall imaging [1–5]. Microwave technology also shows promise in medical diagnostics, since it offers compact low-cost instrumentation and non-ionizing radiation. Many studies have explored the applicability of microwave imaging particularly in breast cancer imaging [6–10]. Another promising venue is the investigation of hybrid imaging methods that involve not only electromagnetic radiation but also acoustic or elastic effects, such as microwave thermoacoustic and photoacoustic imaging [11, 12]. However, microwave imaging has yet to see deployment in clinical practice. The main challenges are rooted in the complex near-field electromagnetic propagation in tissue. Advanced processing techniques are therefore required to create fast and accurate imaging devices for clinicians.

Direct inversion approaches are attractive due to their ability to produce images in real time, simultaneously with measurements. Some examples of direct inversion methods include confocal radar imaging, diffraction tomography, microwave holography, and scattered-power mapping [13–16]. The speed of these methods is due to the linearized models of scattering, which view the observed domain as a collection of uncoupled point scatterers. Two commonly used linear approximations in direct inversion algorithms are Born's approximation (BA) and Rytov's approximation (RA) [17–20]. These methods are known to outperform one another depending on the specifics of the imaging scenario [21].

Quantitative microwave holography (QMH) is a direct inversion approach typically based on BA, but can operate based on RA as well [22]. While microwave holography was originally developed

Received 10 August 2017, Accepted 6 October 2017, Scheduled 20 October 2017

^{*} Corresponding author: Daniel Tajik (tajikd@mcmaster.ca).

The authors are with the McMaster University, Hamilton, Ontario, Canada.

for use in concealed weapons detection [23], the method has recently been adapted for near-field tissue imaging [24]. Further advancements have enabled three-dimensional (3D) quantitative image reconstructions [25–27]. Here, quantitative refers to the ability to estimate the complex permittivity distribution in the object being scanned, rather than estimating only its shape and location. In doing so, QMH presents a unique direct inversion method that can perform differentiation and identification of specific targets, such as cancerous tissue. Moreover, it can be used to provide quantitative contrast information to nonlinear reconstruction algorithms.

In tissue imaging, however, the constraints associated with the linearizing approximations within QMH are strongly violated due to significant mutual coupling and multiple scattering. This may result in image artifacts, the shape and location of which are generally unpredictable. Such artifacts can be avoided only by properly accounting for the nonlinear scattering phenomena, which are not the subject of the current investigation. On the other hand, QMH is also afflicted by image artifacts that are not due to multiple scattering and mutual coupling. The focus here is on eliminating such artifacts. This is imperative before proceeding toward nonlinear QMH reconstruction for tissue imaging.

This work begins with a derivation of the Born and Rytov approximations in the framework of S -parameters. QMH is then introduced with the appropriate algorithmic modifications to allow for operation with either BA or RA. Note that while these modifications were first stated in [22], the current work provides the derivation of Rytov-based QMH (RA-QMH) for the first time. Next, the complications associated with solving the inverse problem in the Fourier domain are stated. Two filtering methodologies, 2D real-domain apodization filtering [28–30] and 2D Fourier domain low-pass filtering are explored. A 3D simulation experiment is considered, demonstrating the importance of filtering. Finally, a 2D tissue experiment shows the ability of QMH to reconstruct permittivity maps in a highly nonlinear scattering scenario. Our investigation suggests that while QMH struggles in such scenarios, it still provides a useful complex permittivity distribution of the inspected tissue object. This distribution is useful in two ways. Firstly, it can serve as the initial guess in a nonlinear reconstruction procedure. Currently, it is customary to set such an initial estimate as the known uniform background medium. We show that QMH can provide a far better object-specific initial estimate. Secondly, due to its remarkable speed, QMH can serve as a quantitative linear-reconstruction module within a nonlinear solver for high-speed tissue imaging.

2. LINEARIZED MODELS OF SCATTERING

The frequency-domain forward model of scattering in dielectric objects is derived from the vector Helmholtz equation for the electric field and can be stated as follows [20]:

$$\mathbf{E}^{\text{sc}}(\mathbf{r}) = \iiint_V k_0^2 \Delta\epsilon_r(\mathbf{r}') \underline{\underline{\mathbf{G}}}_b(\mathbf{r}, \mathbf{r}') \cdot \mathbf{E}^{\text{tot}}(\mathbf{r}') dv', \quad (1)$$

where $\mathbf{E}^{\text{sc}}(\mathbf{r})$ is the scattered electric field at the position of observation \mathbf{r} , V the volume of the imaged domain, k_0 the wavenumber in free space, $\Delta\epsilon_r(\mathbf{r}')$ the complex relative-permittivity contrast $\Delta\epsilon_r = \Delta\epsilon_r' + i\Delta\epsilon_r''$ between the object and the background at the position \mathbf{r}' , $\underline{\underline{\mathbf{G}}}_b(\mathbf{r}, \mathbf{r}')$ the Green's dyadic function, and $\mathbf{E}^{\text{tot}}(\mathbf{r}')$ the total internal electric field. It is useful to formulate (1) as a data equation, on which QMH operates:

$$\overline{\mathbf{E}}^{\text{sc}}(\mathbf{r}) = \iiint_V k_0^2 \Delta\epsilon_r(\mathbf{r}') \underline{\underline{\mathbf{G}}}_b(\mathbf{r}, \mathbf{r}') \cdot \mathbf{E}^{\text{tot}}(\mathbf{r}') dv', \quad \mathbf{r} \notin V, \quad (2)$$

where $\overline{\mathbf{E}}^{\text{sc}}(\mathbf{r})$ is a measured vector value in the dataset.

Note, however, that most microwave measurement systems acquire the scattering parameters (S -parameters) instead of electric-field values. As shown in [31], Eq. (2) can be modified to operate using the scattering component of the S -parameter:

$$S_{ik}^{\text{sc}}(\mathbf{r}) = \frac{i\omega\epsilon_0}{2a_i a_k} \iiint_V \Delta\epsilon_r(\mathbf{r}') [\mathbf{E}_i^{\text{inc}} \cdot \mathbf{E}_k^{\text{tot}}](\mathbf{r}', \mathbf{r}) dv', \quad (3)$$

where $\omega = 2\pi f$ is the angular frequency, and a_ζ ($\zeta = i, k$) is the incoming root power wave at the ζ -th

antenna port[†]. The scattering component of an S -parameter is the one associated with the scattered field $\overline{\mathbf{E}}^{\text{sc}}$ at the location of the receiving antenna. Note that in (3), Green's dyadic function has been replaced with the scaled electric field $\mathbf{E}_i^{\text{inc}}$ of the receiving (i -th) antenna when it operates in a transmitting mode. The electric field dot product $[\mathbf{E}_i^{\text{inc}} \cdot \mathbf{E}_k^{\text{tot}}](\mathbf{r}', \mathbf{r})$, referred to as the resolvent kernel, is a function of the observation position \mathbf{r} and the position within the imaged volume \mathbf{r}' .

The scattering integral equation (3) is nonlinear with respect to the permittivity contrast due to the implicit dependence of $\mathbf{E}_k^{\text{tot}}(\mathbf{r}', \mathbf{r})$ on the permittivity contrast in V . In the case of weak scattering, the first-order Born approximation can be applied so that $\mathbf{E}_k^{\text{tot}}(\mathbf{r}', \mathbf{r})$ is replaced by the incident electric field $\mathbf{E}_k^{\text{inc}}(\mathbf{r}', \mathbf{r})$ [18]:

$$S_{ik}^{\text{sc}}(\mathbf{r}) \approx \frac{i\omega\epsilon_0}{2a_i a_k} \iiint_V \Delta\epsilon_r(\mathbf{r}') [\mathbf{E}_i^{\text{inc}} \cdot \mathbf{E}_k^{\text{inc}}](\mathbf{r}', \mathbf{r}) dv'. \quad (4)$$

Equation (4) gives the forward model of QMH. This linearization ignores the multiple scattering that may occur within the imaged domain. This implies that the permittivity contrast $\Delta\epsilon_r(\mathbf{r}')$ is minimal. With the forward model linearized and in an S -parameter form, the differences between BA and RA can now be highlighted.

2.1. Born's Approximation

Note that the scattered portion of the S -parameter $S_{ik}^{\text{sc}}(\mathbf{r})$ cannot be measured directly but it can be derived from the measured $S_{ik}^{\text{inc}}(\mathbf{r})$ and $S_{ik}^{\text{tot}}(\mathbf{r})$ responses. Here, S_{ik}^{inc} is the S -parameter measurement in the absence of scatterers (often referred to as the baseline measurement), and S_{ik}^{tot} is the S -parameter measurement of the object to be reconstructed. Born's approximation views $S_{ik}^{\text{tot}}(\mathbf{r})$ as the superposition of $S_{ik}^{\text{sc}}(\mathbf{r})$ and $S_{ik}^{\text{inc}}(\mathbf{r})$ [18–20], which allows Equation (4) to be expressed as:

$$[S_{ik}^{\text{sc}}(\mathbf{r})]_{\text{BA}} = S_{ik}^{\text{tot}}(\mathbf{r}) - S_{ik}^{\text{inc}}(\mathbf{r}) \approx \frac{i\omega\epsilon_0}{2a_i a_k} \iiint_V \Delta\epsilon_r(\mathbf{r}') [\mathbf{E}_i^{\text{inc}} \cdot \mathbf{E}_k^{\text{inc}}](\mathbf{r}', \mathbf{r}) dv'. \quad (5)$$

Note that Eq. (5) is linear with respect to the unknown $\Delta\epsilon_r(\mathbf{r}')$. It is well known that such a linearizing approximation ignores multiple scattering and mutual coupling effects.

A major limitation of BA is its sensitivity to errors in the overall phase of the total field as it propagates through an object [21, 32–34]. To keep these errors small, the following constraint must be observed:

$$2asup |k_s(\mathbf{r}') - k_b| < \pi, \quad \mathbf{r}' \in V. \quad (6)$$

Here a is the radius of the smallest sphere that circumscribes the scatterer, k_s the wavenumber of the scatterer, and k_b the wavenumber in the background medium. Note that the above limitation associated with the Born approximation applies to the observed external field and the respective S -parameters. A stricter limitation exists in the case where the integral equation of scattering is applied to the internal field, i.e., when $\mathbf{r} \in V$ [21].

2.2. Rytov's Approximation

Rytov's approximation views the total field as a complex-phase correction to the incident field [18, 19, 21],

$$S_{ik}^{\text{tot}}(\mathbf{r}) \approx S_{ik}^{\text{inc}}(\mathbf{r}) \cdot \exp\left(\frac{S_{ik}^{\text{sc}}(\mathbf{r})}{S_{ik}^{\text{inc}}(\mathbf{r})}\right). \quad (7)$$

To form the Rytov forward model, the above equation is rearranged and substituted into Eq. (4), leading to

$$[S_{ik}^{\text{sc}}(\mathbf{r})]_{\text{RA}} = S_{ik}^{\text{inc}}(\mathbf{r}) \cdot \ln\left(\frac{S_{ik}^{\text{tot}}(\mathbf{r})}{S_{ik}^{\text{inc}}(\mathbf{r})}\right) \approx \frac{i\omega\epsilon_0}{2a_i a_k} \iiint_V \Delta\epsilon_r(\mathbf{r}') [\mathbf{E}_i^{\text{inc}} \cdot \mathbf{E}_k^{\text{inc}}](\mathbf{r}', \mathbf{r}) dv'. \quad (8)$$

[†] If the field phasors $\mathbf{E}_i^{\text{inc}}$ and $\mathbf{E}_k^{\text{tot}}$ in (3) are RMS phasors, then a_ζ is equal to the square root of the power launched toward the ζ -th port by the ζ -th transmitter.

The central portion of Eq. (8) forms the data vector in the RA-QMH reconstruction whereas the right-hand side is the same as that of the BA-based QMH (BA-QMH); see Eq. (5). Note that Eq. (8), similar to Eq. (5), is also a linear integral equation with respect to the unknown $\Delta\epsilon_r(\mathbf{r}')$.

The limitation of RA is that there must be minimal phase change across a single wavelength [21, 34]. This has been shown to translate into the requirement:

$$\left| \frac{\mu_s \epsilon_s - \mu_b \epsilon_b}{\mu_b \epsilon_b} \right| < 1. \quad (9)$$

It has been shown that the above limitation associated with the linear Rytov approximation must be observed not only for the external fields (and the measured S -parameters) but also for any internal-field scattering models [21]. Note that, unlike the constraint of BA stated in Eq. (6), RA does not depend on the size of the scatterer. It is also important to note that both methods still depend on a low-contrast imaging scene, and converge to the same solution as the permittivity contrast decreases.

3. RYTOV-BASED QUANTITATIVE MICROWAVE HOLOGRAPHY

3.1. Forward Model Based on Measurements

Near-field microwave holography based on BA has been derived in [24, 26]. There it is emphasized that the success of near-field holography depends critically on the fidelity of the forward model. It is shown that sufficient fidelity is achievable through calibration measurements, whereas analytical approximations and simulations (such as those used in far-field imaging) often fail to accurately model the particular acquisition setup. Quantitative BA-based microwave holography has been proposed in [22, 25]. To our knowledge, RA-QMH is derived for the first time here.

QMH depends on the measurement of three separate datasets known as the reference object (RO), the calibration object (CO), and the object under test (OUT). The first two measurements are part of the system calibration. The RO is the background without scattering objects. Its measurement provides the incident-field (or baseline) responses $S_{ik}^{\text{RO}}(\mathbf{r}) \equiv S_{ik}^{\text{inc}}(\mathbf{r})$. The CO is the same as the RO except for an electrically small scatterer of known permittivity contrast $\Delta\epsilon_{r,\text{sp}}$ embedded in the center $\mathbf{r}'_0 = (0, 0, 0)$ of V . The so acquired S -parameters $S_{ik}^{\text{CO}}(\mathbf{r}, \mathbf{r}'_0)$ represent the system point-spread functions (PSFs). Finally, the measurement of the OUT provides $S_{ik}^{\text{OUT}}(\mathbf{r})$. Both the CO and the OUT data, $S_{ik}^{\text{CO}}(\mathbf{r}, \mathbf{r}'_0)$ and $S_{ik}^{\text{OUT}}(\mathbf{r})$, represent total-field responses. These three dataset acquisitions are illustrated in Figure 1.

We consider an acquisition system that performs a planar raster scan along the x and y axes. The sampling positions are indexed by $m = 1, \dots, N_x$ and $n = 1, \dots, N_y$ along x and y , respectively. At each sampling position, the measurement involves N_r receiving (Rx) antennas and N_t transmitting (Tx) antennas, indexed by $i = 1, \dots, N_r$ and $k = 1, \dots, N_t$, respectively. Thus, the number of acquired S -parameters is $N_s = N_r \times N_t$, where each measurement is indexed by $p = 1, \dots, N_s$. The data at each measurement are captured one frequency f_u at a time, indexed by $u = 1, \dots, N_f$. Finally, the discretization of the imaged domain utilizes a uniform grid of $N_v = N_x \times N_y \times N_z$ voxels, each of volume Ω_v as shown in Figure 2.

Assuming sufficient sampling, the S -parameter data can be expressed as a function of the continuous variables x , y , and f as $S_{ik}(\mathbf{r}; f) = S_{ik}(x, y, \bar{z}; f)$. Note that the constant position \bar{z} is that of the acquisition plane scanned by the receiving antenna.

Solving the forward model stated in Eq. (8) requires the resolvent kernel $[\mathbf{E}_i^{\text{inc}} \cdot \mathbf{E}_k^{\text{inc}}](\mathbf{r}', \mathbf{r}; f)$, which is unknown. However, it can be derived from the PSF $S_{ik}^{\text{CO}}(\mathbf{r}, \mathbf{r}'_0; f)$. Consider the contrast function $\Delta\epsilon_r^{\text{CO}}(x', y', z')$ of a CO when the scattering probe is placed at $\mathbf{r}'_{\text{sp}} = (x'_{\text{sp}}, y'_{\text{sp}}, 0)$. Since the permittivity contrast $\Delta\epsilon_{r,\text{sp}}$ of the scattering probe is known, $\Delta\epsilon_r^{\text{CO}}(x', y', z')$ is expressed as:

$$\Delta\epsilon_r^{\text{CO}}(x', y', z') = \delta(x' - x'_{\text{sp}}, y' - y'_{\text{sp}}, z') \Delta\epsilon_{r,\text{sp}} \Omega_{\text{sp}}. \quad (10)$$

Here, δ is the 3D Dirac delta function, and Ω_{sp} is the volume of the scattering probe. Using Eqs. (8) and (10), along with the sampling property of the δ function, the probe's scattering response is obtained as:

$$\left[S_{ik}^{\text{sc,CO}}(\mathbf{r}, \mathbf{r}'_{\text{sp}}; f) \right]_{\text{RA}} \approx \frac{i\omega\epsilon_0}{2a_i a_k} \Delta\epsilon_{r,\text{sp}} \Omega_{\text{sp}} [\mathbf{E}_i^{\text{inc}} \cdot \mathbf{E}_k^{\text{inc}}](\mathbf{r}'_{\text{sp}}, \mathbf{r}; f), \quad (11)$$

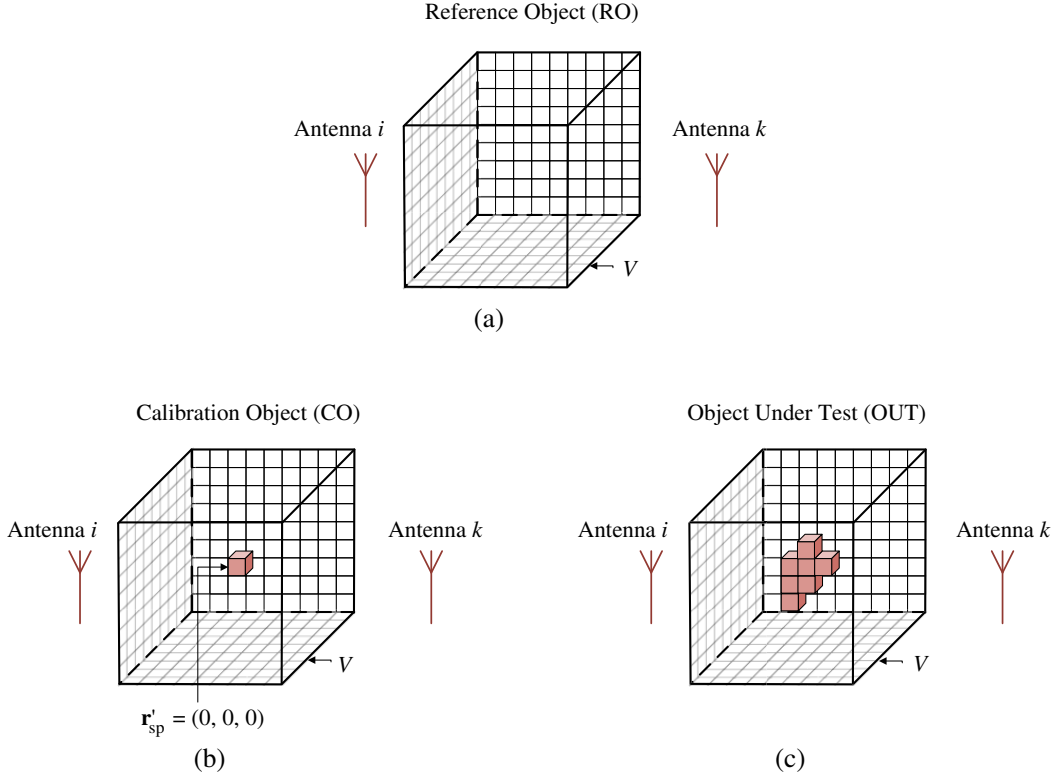


Figure 1. Illustrations of the three datasets required for the QMH reconstruction. (a) The RO measurement provides the incident-field data. It is the measurement in the absence of scatterers. (b) The CO yields the total-field system PSF. It is a measurement with a scattering probe at the center of the imaged volume. (c) The OUT S -parameters comprise the total-field data, and are acquired by measuring the object under test.

where

$$\left[S_{ik}^{\text{sc,CO}}(\mathbf{r}, \mathbf{r}'_{\text{sp}}; f) \right]_{\text{RA}} = S_{ik}^{\text{RO}}(\mathbf{r}; f) \cdot \ln \left(\frac{S_{ik}^{\text{CO}}(\mathbf{r}, \mathbf{r}'_{\text{sp}}; f)}{S_{ik}^{\text{RO}}(\mathbf{r}; f)} \right), \quad (12)$$

is the Rytov approximation of the probe's scattering response.

Equation (11) can be rearranged as:

$$\frac{i\omega\epsilon_0}{2a_i a_k} [\mathbf{E}_i^{\text{inc}} \cdot \mathbf{E}_k^{\text{inc}}](\mathbf{r}'_{\text{sp}}, \mathbf{r}; f) \approx \frac{S_{ik}^{\text{sc,CO}}(\mathbf{r}, \mathbf{r}'_{\text{sp}}; f)}{\Delta\epsilon_{\text{r,sp}}\Omega_{\text{sp}}}. \quad (13)$$

The dot product $[\mathbf{E}_i^{\text{inc}} \cdot \mathbf{E}_k^{\text{inc}}](\mathbf{r}'_{\text{sp}}, \mathbf{r}; f)$ in Eq. (13) is exactly the resolvent kernel of the forward model in Eq. (8), provided $\mathbf{r}'_{\text{sp}} = \mathbf{r}'$. Thus, a PSF for every position $\mathbf{r}' \in V$ is required to generate the full resolvent kernel.

Assume that the background medium is translationally invariant along the lateral axes x and y . Then, the measured PSF with the scattering probe at $\mathbf{r}'_{\text{sp}} = (x'_{\text{sp}}, y'_{\text{sp}}, 0)$ can be obtained via coordinate translation of the PSF with the scattering probe at the center $\mathbf{r}'_0 = (0, 0, 0)$:

$$S_{ik}^{\text{CO}}(x, y, \bar{z}; x'_{\text{sp}}, y'_{\text{sp}}, 0; f) = S_{ik}^{\text{CO}}(x - x'_{\text{sp}}, y - y'_{\text{sp}}, \bar{z}; 0, 0, 0; f). \quad (14)$$

It follows that the resolvent kernel can be expressed as:

$$\frac{i\omega\epsilon_0}{2a_i a_k} [\mathbf{E}_i^{\text{inc}} \cdot \mathbf{E}_k^{\text{inc}}](x', y', 0, x, y, \bar{z}; f) \approx \frac{S_{ik}^{\text{sc,CO}}(x - x', y - y', \bar{z}; \mathbf{r}'_0; f)}{\Delta\epsilon_{\text{r,sp}}\Omega_{\text{sp}}}. \quad (15)$$

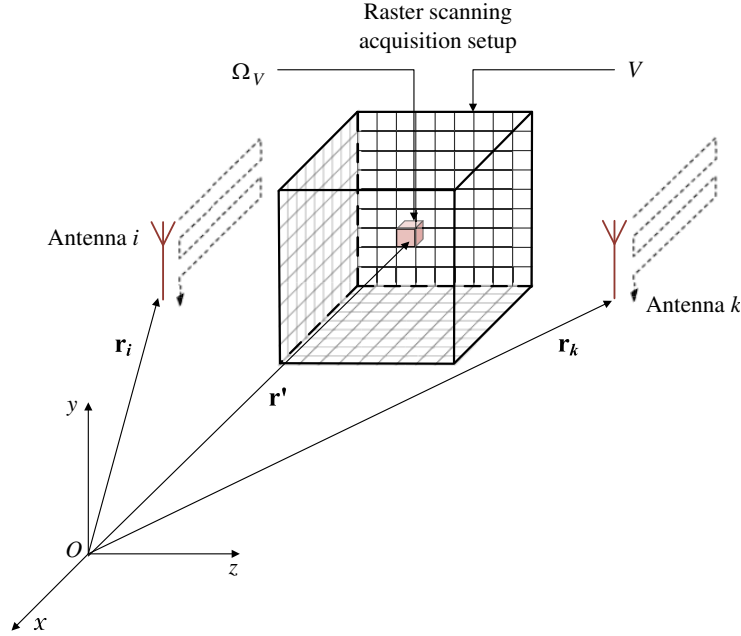


Figure 2. Illustration of a planar raster acquisition scan and the associated notations. A location in the imaged target is denoted with \mathbf{r}' , whereas the locations of the receiving and transmitting antennas are denoted as \mathbf{r}_i and \mathbf{r}_k , respectively. V is the volume of the imaged domain, which is discretized uniformly into N_v voxels of volume Ω_v .

Further, by performing multiple CO measurements with the scattering probe being at different range locations z' , the method is easily extended to reconstruct 3D images slice by slice. The typical sampling rate along z' is chosen to be close to the well-known range resolution limit for far-zone measurements [15]:

$$\Delta z' \approx \frac{v_b}{2 \cdot \text{BW}}, \quad (16)$$

where v_b is the speed of light in the background, and BW is the radiation frequency bandwidth. Denser sampling is also possible, provided the respective N_z PSFs are available. However, significant oversampling along range should be avoided. PSFs measured with the probe closely spaced become linearly dependent, leading to poorly conditioned system matrices. Thus, the sampling along z is typically selected to narrowly match the range resolution limit in Eq. (16).

The scattering equation for the OUT measurement is

$$S_{ik}^{\text{sc},\text{OUT}}(x, y, \bar{z}; f) \approx \iiint_V \Delta \epsilon_r(x', y', z') \frac{i\omega \epsilon_0}{2a_i a_k} [\mathbf{E}_i^{\text{inc}} \cdot \mathbf{E}_k^{\text{inc}}](x', y', z'; x, y, \bar{z}; f) dv'. \quad (17)$$

If the same acquisition setup is used, the resolvent kernel and the associated scaling parameters shown in Equation (15) can be substituted into Equation (17) to obtain

$$S_{ik}^{\text{sc},\text{OUT}}(x, y, \bar{z}; f) \approx \iiint_V \Delta \epsilon_r(x', y', z') \frac{S_{ik}^{\text{sc},\text{CO}}(x - x', y - y', \bar{z}; \mathbf{r}'_0; f)}{\Delta \epsilon_{r,\text{sp}} \Omega_{\text{sp}}} dv'. \quad (18)$$

The inversion process is performed on a discretized volume (see Figure 2). The integration is therefore reduced to a summation over the discrete 3D grid introduced in Section 3.1,

$$S_{ik}^{\text{sc},\text{OUT}}(x_\mu, y_\nu, \bar{z}; f_u) \approx \sum_{q=1}^{N_z} \sum_{m=1}^{N_x} \sum_{n=1}^{N_y} \Delta \epsilon_r(x'_m, y'_n, z'_q) \frac{S_{ik}^{\text{sc},\text{CO}}(x_\mu - x'_m, y_\nu - y'_n, \bar{z}; 0, 0, z'_q; f_u)}{\Delta \epsilon_{r,\text{sp}} \Omega_{\text{sp}}} \Omega_v, \quad (19)$$

$$\mu = 1, \dots, N_x, \quad \nu = 1, \dots, N_y.$$

The forward data model is now reduced to a form that operates purely on measured data.

It is important to note that Tu et al. proved that the forward model can be improved through the use of the localized nonlinear and quasi-analytic approximations [15, 18]. The improvement, however, is marginal. It was also shown that quantitative reconstruction is better if the contrast of the scattering probe is close to that of the OUT.

In wideband data acquisitions, both the OUT and CO datasets are normalized according to the strongest response $|S_{ik}^{\text{sc,CO}}(x_\mu, y_\nu, \bar{z}; 0, 0, z'_q; f_u)|$ at any given frequency, i.e.,

$$\bar{S}_{ik}^{\text{sc,OBJ}}(x_\mu, y_\nu, \bar{z}; f_u) = \frac{S_{ik}^{\text{sc,OBJ}}(x_\mu, y_\nu, \bar{z}; f_u)}{\max_{\mathbf{r}} |S_{ik}^{\text{sc,CO}}(x_\mu, y_\nu, \bar{z}; 0, 0, z'_q; f_u)|}, \text{OBJ} \equiv \text{OUT, CO.} \quad (20)$$

Note that this normalization does not affect the stability of the inversion since it occurs in the spatial domain. Thus, it does not impact the illposedness of the system matrix in the Fourier domain. In tissue, the signals at the higher frequencies tend to be substantially weaker than those at lower frequencies due to the increase of loss. Normalization is desirable because it creates equal weighting of the responses across all frequencies during the inversion process.

3.2. Inversion Procedure

The double sum over x'_m and y'_n in Eq. (19) is a convolution. A 2D Fourier transform is applied to change the convolution into a multiplication:

$$\tilde{S}_{ik}^{\text{sc,OUT}}(\boldsymbol{\kappa}, \bar{z}; f_u) \approx \sum_{q=1}^{N_z} \frac{\Omega_v \Delta \tilde{\epsilon}_r(\boldsymbol{\kappa}, z'_q)}{\Delta \epsilon_{r,\text{sp}} \Omega_{\text{sp}}} \tilde{S}_{ik}^{\text{sc,CO}}(\boldsymbol{\kappa}, z'_q; f_u). \quad (21)$$

Here $\boldsymbol{\kappa} = (\kappa_x, \kappa_y)$ denotes a position in the Fourier space. The quantitative factors are combined with the contrast function to form the reflectivity function,

$$\tilde{\rho}(\boldsymbol{\kappa}, z'_q) = \frac{\Omega_v}{\Delta \epsilon_{r,\text{sp}} \Omega_{\text{sp}}} \Delta \tilde{\epsilon}_r(\boldsymbol{\kappa}, z'_q), \quad (22)$$

which, when substituted into Eq. (21), yields:

$$\tilde{S}_p^{\text{sc,OUT}}(\boldsymbol{\kappa}, \bar{z}; f_u) \approx \sum_{q=1}^{N_z} \tilde{\rho}(\boldsymbol{\kappa}, z'_q) \tilde{S}_p^{\text{sc,CO}}(\boldsymbol{\kappa}, z'_q; f_u), \quad (23)$$

where $p = 1 \dots N_s$ is an S -parameter experiment (i, k). At each p -th experiment, Equation (23) is a system of linear equations at each spectral position $\boldsymbol{\kappa}$:

$$\tilde{\mathbf{A}}(\boldsymbol{\kappa}) \tilde{\boldsymbol{\rho}}(\boldsymbol{\kappa}) = \tilde{\mathbf{b}}(\boldsymbol{\kappa}), \quad (24)$$

where

$$\tilde{\mathbf{A}}(\boldsymbol{\kappa}) = \begin{bmatrix} \tilde{S}_p^{\text{sc,CO}}(\boldsymbol{\kappa}, f_1, z_1) & \dots & \tilde{S}_p^{\text{sc,CO}}(\boldsymbol{\kappa}, f_1, z_{N_z}) \\ \vdots & \ddots & \vdots \\ \tilde{S}_p^{\text{sc,CO}}(\boldsymbol{\kappa}, f_{N_f}, z_1) & \dots & \tilde{S}_p^{\text{sc,CO}}(\boldsymbol{\kappa}, f_{N_f}, z_{N_z}) \end{bmatrix}, \quad (25)$$

$$\tilde{\boldsymbol{\rho}}(\boldsymbol{\kappa}) = \begin{bmatrix} \tilde{\rho}(\boldsymbol{\kappa}, z_1) \\ \vdots \\ \tilde{\rho}(\boldsymbol{\kappa}, z_{N_z}) \end{bmatrix}, \quad (26)$$

$$\tilde{\mathbf{b}}(\boldsymbol{\kappa}) = \begin{bmatrix} \tilde{S}_p^{\text{sc,OUT}}(\boldsymbol{\kappa}, f_1) \\ \vdots \\ \tilde{S}_p^{\text{sc,OUT}}(\boldsymbol{\kappa}, f_{N_f}) \end{bmatrix}. \quad (27)$$

In a scenario where multiple S -parameters are acquired, the system and data matrices become:

$$\tilde{\mathbf{A}}(\boldsymbol{\kappa}) = \begin{bmatrix} \tilde{S}_1^{\text{sc,CO}}(\boldsymbol{\kappa}) \\ \vdots \\ \tilde{S}_{N_s}^{\text{sc,CO}}(\boldsymbol{\kappa}) \end{bmatrix}, \quad (28)$$

$$\tilde{\mathbf{b}}(\boldsymbol{\kappa}) = \begin{bmatrix} \tilde{S}_1^{\text{sc,OUT}}(\boldsymbol{\kappa}) \\ \vdots \\ \tilde{S}_{N_s}^{\text{sc,OUT}}(\boldsymbol{\kappa}) \end{bmatrix}. \quad (29)$$

The inversion can therefore be expressed as:

$$\tilde{\rho}(\boldsymbol{\kappa}) = [\tilde{\mathbf{A}}(\boldsymbol{\kappa})]^\dagger \cdot \tilde{\mathbf{b}}(\boldsymbol{\kappa}), \quad (30)$$

where \dagger denotes pseudoinverse. The necessity of the pseudoinverse is due to the rank-deficiency of the typical system matrix $\tilde{\mathbf{A}}(\boldsymbol{\kappa})$. There are more frequency samples along f than range samples along z' , i.e., $N_f > N_z$. The minimum number of frequency samples is dictated by the need to prevent aliasing between frequencies; thus, the frequency step size is limited to [21]:

$$\Delta f < \frac{v_b}{4R_{\max}}. \quad (31)$$

Here, v_b is the speed of light in the background medium, and R_{\max} is the maximum distance from the antenna to a target in the imaged domain. Note that the frequency step is selected near the limit to avoid oversampling and thus illposedness in the inversion. This strategy is similar to the one used for determining the z' sampling step, shown in Eq. (16). In tissue measurements, the differences between Eqs. (16) and (31) typically leads to a larger number of frequency measurements than the maximum number of linearly independent z' -plane measurements.

For example, consider a measurement in the imaging of a compressed breast tissue of a thickness of 5 cm. If the averaged relative permittivity of the breast can be assumed to be $\epsilon_r \approx 10 - i5$, and the distance from the farthest extent of the breast to the antenna is 7.5 cm, the frequency sampling step from Eq. (31) is determined to be $\Delta f = 307$ MHz.

On the other hand, to achieve a range resolution of 1 cm (i.e., 5 independent z' -planes), a frequency bandwidth of 4.60 GHz is required; see Eq. (16). For this particular setup, at least 15 frequency samples are required in order to avoid violating the constraints of frequency sampling stated in Eq. (31). Thus, in this common scenario, $N_f > N_z$, and the resultant system matrix $\tilde{\mathbf{A}}(\boldsymbol{\kappa})$ is overdetermined.

The solution of Eq. (30), $\tilde{\rho}(\boldsymbol{\kappa}, z'_q)$, $q = 1, \dots, N_z$, is found for all $\boldsymbol{\kappa} = (\kappa_x, \kappa_y)$. Then the inverse 2D Fourier transform is applied to each z' -plane of the reflectivity function to obtain $\rho(x', y', z')$ over the discretized volume $N_x \times N_y \times N_z$. The multiplicative factors are finally applied to calculate the relative complex permittivity of the OUT:

$$\epsilon_{r,\text{OUT}}(x, y, z) \approx \rho(x, y, z) \cdot \Delta\epsilon_{r,\text{sp}} \frac{\Omega_{\text{sp}}}{\Omega_v} + \epsilon_{r,b}. \quad (32)$$

It is critical to note that the differences between the Born and Rytov approximations are solely related to the approximation of the scattered field data. Since these modifications are all applied before the inversion stage and operate on the same dataset, RA-QMH can compute the reconstruction at the same speed as BA-QMH, which typically takes several seconds [22, 25, 27].

4. FILTERING STRATEGIES

Proper data filtering is critical to ensure successful reconstruction via QMH. Without filtering, ringing artifacts and high-frequency noise obscure the target in the image. Two strategies, apodization filtering in the real (x, y) domain and post-inversion low-pass filtering in the Fourier domain, are used to improve reconstruction quality while preserving quantitative output.

4.1. Apodization Filtering

Apodization (or edge) filtering is used in photography, ultrasound imaging, and magnetic resonance imaging (MRI) [35–38]. It removes the presence of ringing artifacts that are generated by the DFT. The issue arises because the DFT assumes that parallel edges of an image are continuous with respect to one another, e.g., the left side of an image can be wrapped around to the right side resulting in a smooth transition. However, in physical measurements, the edges are frequently different due to

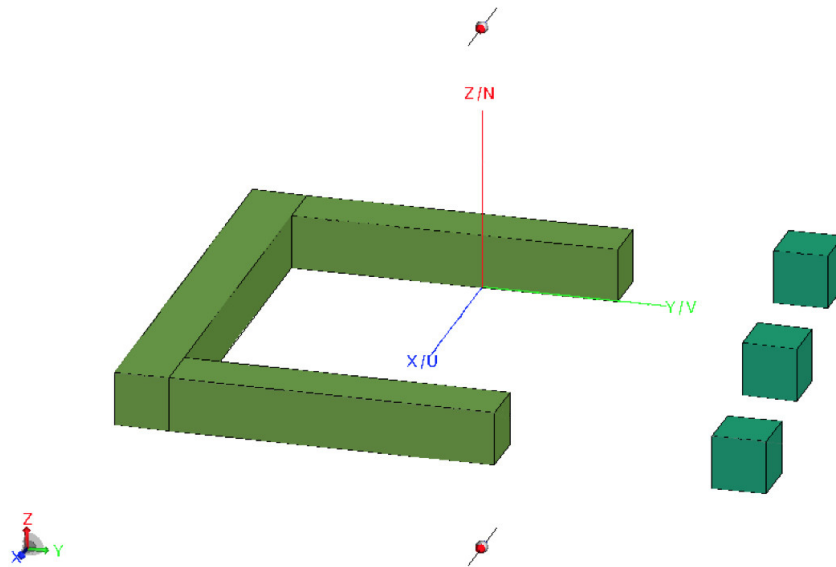


Figure 3. The scattering object (OUT) in the simulation example. A C-shaped object of dielectric permittivity $\epsilon_r = 1.5 - i0$ is placed in a plane which is 4 cm away from the lower dipole antenna. Three scattering cubes ($\epsilon_r = 1.1 - i0$) of side length 1 cm are placed along z' at distances 4 cm, 5 cm, and 6 cm away from the lower antenna. They are also displaced by 1 cm along the x -axis with respect to each other. The two antennas are aligned along boresight and sweep across the 30 cm by 30 cm acquisition plane at 1 cm intervals. The background medium is vacuum.

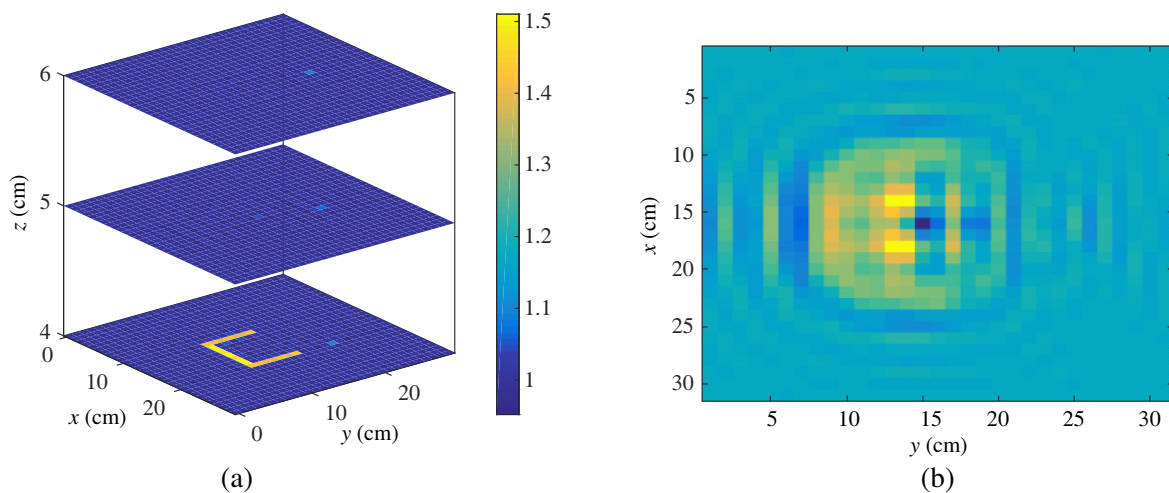


Figure 4. (a) Reconstruction of the real part of the permittivity of the simulated OUT using RA-QMH. The quantitative values of the C-shape and the smaller scattering targets are estimated accurately. (b) The magnitude of the data of the OUT simulated at 8 GHz.

noise and hardware discontinuities. This edge discontinuity causes the DFT to generate artifacts in the Fourier domain. These artifacts are related to Gibb’s phenomenon, where large discontinuities create sinc-function ringing in the 2D Fourier domain [39]. This ringing is amplified during the inversion stage, creating point and cross-like artifacts in the final images.

There are a variety of apodization filters that can be used to remove these artifacts, including simple Gaussian functions, the Happ-Genzel filter, and tapered edge techniques [37, 38]. For the sake of simplicity, a simple cosine function is used here to demonstrate the ability of apodization filtering to improve the image quality.

Figure 3 shows a C-shape scattering object along with three small cubes in a background of vacuum. The data in this example is acquired through simulations with the commercial CAD package FEKO [40]. The letter “C”, of dielectric permittivity $\epsilon_r = 1.5 - i0$, is placed on a plane between two dipole antennas which are aligned along boresight and are 10 cm apart. The C-shaped object is positioned 4 cm away from the lower antenna along z . There are also 3 small 1 cm^3 cubes of $\epsilon_r = 1.1 - i0$ that are placed on different z' -planes at distances of 4 cm, 5 cm, and 6 cm from the lower antenna. Each of these small scattering objects are also offset by 1 cm along the x axis with respect to each other. To generate 3D images, three CO measurements are acquired with a scattering probe placed in the center of the 2D slices of the region of interest (ROI) at z' of 4 cm, 5 cm, and 6 cm away from the lower antenna. The ROI is a volume of extent 30 cm along x' and y' and 10 cm along z' . Reconstruction is only performed on the planes where objects are located at, i.e., 4 cm, 5 cm, and 6 cm away from the lower antenna. The permittivity of the scattering probe in the CO is $\epsilon_r = 1.1 - i0$. The S -parameters are acquired across a 30 cm by 30 cm acquisition plane at 1 cm intervals. A frequency range from 3 GHz to 8 GHz is swept in 1 GHz increments. Note that the limitations stated in (9), (16), and (31) are observed.

The results of the RA-QMH reconstruction without any filtering can be seen in Figure 4(a). The C-shaped object is clearly reconstructed along with accurate quantitative values. The locations and permittivities of the smaller scattering objects are also determined accurately. While there are some minor ringing artifacts, they barely affect the image. Note that here the edges of the OUT datasets have nearly identical values, as shown in Figure 4(b) for the case of 8 GHz.

Now consider a QMH reconstruction with a seemingly insignificant discontinuity at the edge of the image domain, such as the one shown in Figure 5(a). Such discontinuities are common in experimental measurements. The small Gaussian disturbance shown in Figure 5(a) is artificially added to the simulated OUT dataset at each frequency. With these data, QMH produces noisy results throughout

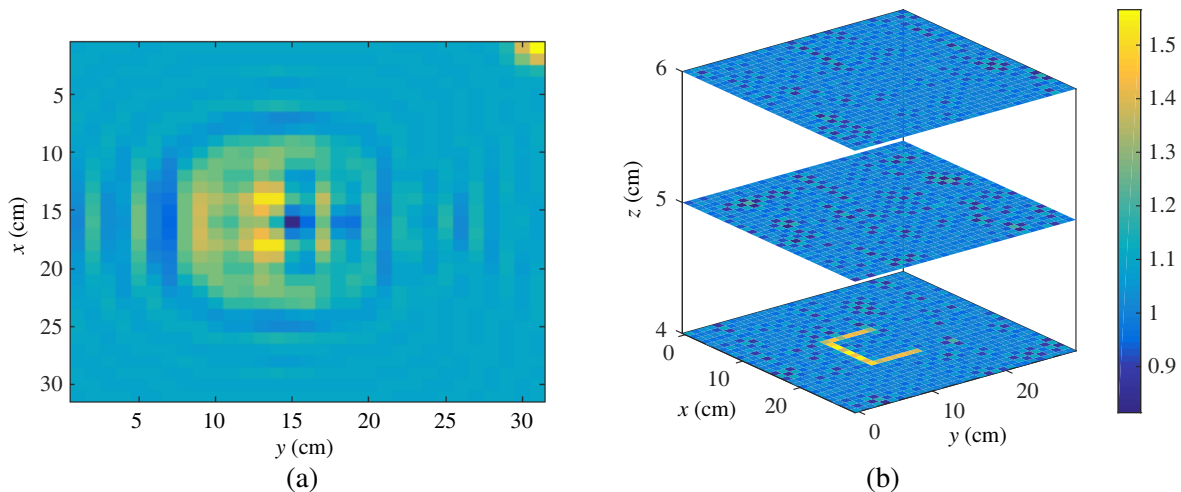


Figure 5. (a) The magnitude of the data of the OUT simulated at 8 GHz, with a small Gaussian-shaped signal disturbance added artificially to the top right corner of the acquisition plane. (b) Reconstruction of the real part of the permittivity of the simulated OUT using RA-QMH, when the same small Gaussian-shaped disturbance shown in (a) is added to the data at each frequency. While the quantitative estimate of the C-shape permittivity is reasonable, the smaller scattering objects are not visible in the noisy image.

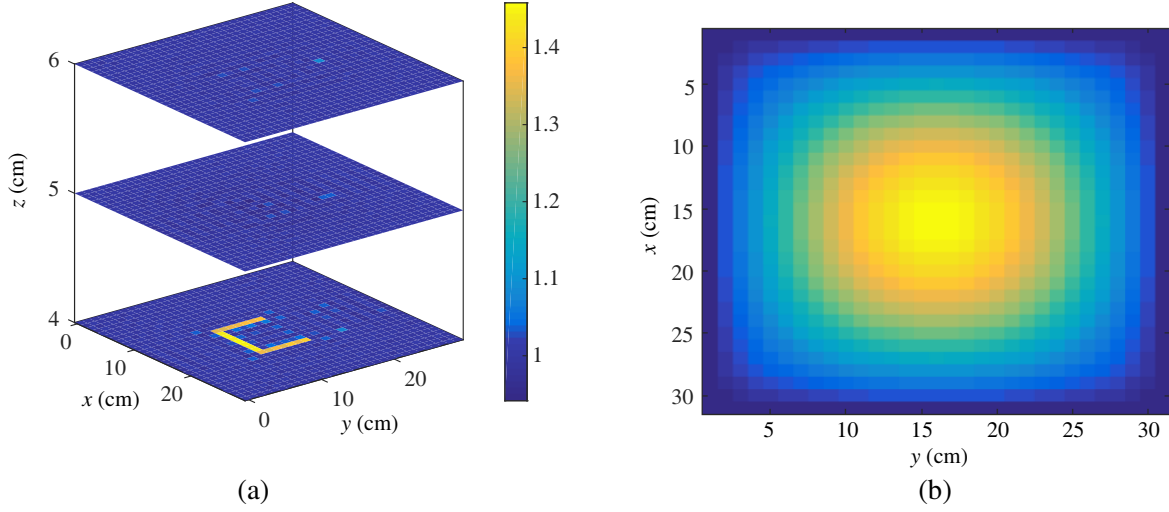


Figure 6. (a) Reconstruction of the real part of the permittivity of the simulated OUT using RA-QMH, when the data is corrupt with the corner disturbance. A cosine apodization filter is used to reduce the impact of the disturbance. (b) The apodization filter based on a 2D cosine distribution across the entire acquisition plane.

the imaged volume (Figure 5(b)). While the C-shape is discernible, the smaller scattering objects are not visible and nonphysical values ($\epsilon'_r < 1$) are present. To correct this error, an apodization filter based on a 2D cosine function is applied to the scattered responses of the OUT and CO datasets (Figure 6(b)). As shown in Figure 6(a), a clearer image is reconstructed, with the small scattering objects made visible. The quantitative results are accurate as well.

In actual imaging measurements, noise and discontinuities at the edges of the image domain are common due to reflections from the enclosures and/or the components of the positioning mechanism. This is why apodization is a necessity. This is especially important in tissue imaging where, in addition to strong edge discontinuities, we also deal with low signal-to-noise ratio (SNR).

4.2. Post-Inversion Low-Pass Filtering

Another common cause of artifacts is oversampling along x and y . Oversampling is typically used in experimental measurements to improve the resolution and to reduce the impact of measurement noise. For far-zone measurements, the following lateral sampling step is recommended [21]:

$$\Delta\zeta < \Delta\zeta_{\max} \approx \frac{\lambda_{\min}}{4 \sin \alpha_{\max}}, \quad \zeta \equiv x, y, \quad (33)$$

where α_{\max} is the maximum angle at which the antenna “sees” the OUT. This is either the angle between the axis of the antenna and the far edge of the OUT, or one-half of the antenna beamwidth, whichever is smaller (Figure 7(a) depicts the latter situation). Equation (33) is derived from the maximum spatial variation that can occur in κ_{ζ} with far-zone data, which is,

$$\kappa_{\zeta}^{\max} \approx \frac{4\pi \sin \alpha_{\max}}{\lambda_{\min}}. \quad (34)$$

Note, however, that the spatial signal variation with near-field measurements may be more rapid, leading to higher spatial frequencies κ_x or κ_y . Consider an acquisition which uses a sampling step $\Delta\zeta$ several times smaller than the limit $\Delta\zeta_{\max}$ in Eq. (33). The DFT then generates a spatial frequency range $\pm\pi/\Delta\zeta$ which is much larger than the limit stated in Eq. (34) ($\pi/\Delta\zeta > \kappa_{\zeta}^{\max}$). With weak or absent near-field data, the spectral components outside of the circle of radius κ_{ζ}^{\max} in Fourier space contains mostly noise, which leads to high-frequency artifacts appearing in the reconstructed images.

To handle this, a wide variety of low-pass filters exist. For the purposes of this work, a simple Butterworth filter is selected. It is designed to ensure that its 3 dB cut-off spatial frequency matches

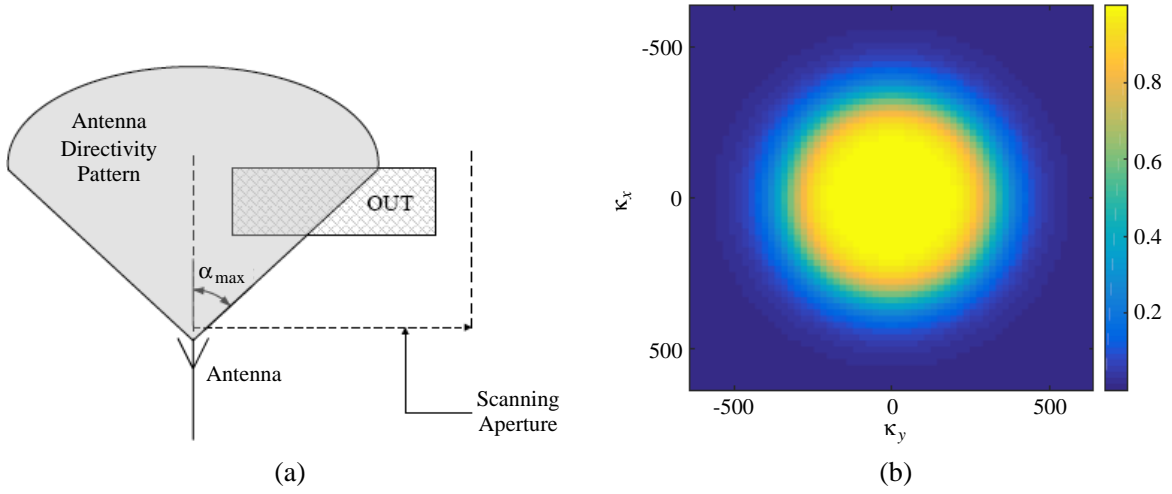


Figure 7. (a) Example of how α_{\max} is limited by the antenna directivity pattern. This limitation arises because the antenna pattern does not cover the entirety of the OUT. In the case where the antenna pattern covers the entire OUT, α_{\max} becomes the angle between the antenna axis and the farthest corner of the OUT. (b) Fourth-order Butterworth filter whose cut-off frequency has been set to k_{\max} .

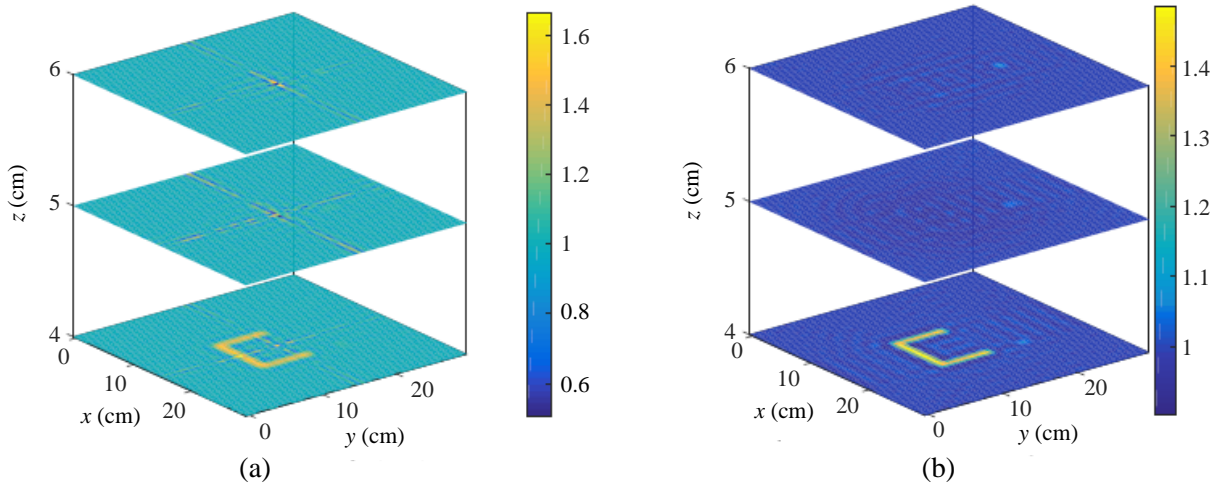


Figure 8. (a) Simulation reconstruction of the real part of the permittivity with oversampled raw data. (b) Reconstruction of the real part of the permittivity of the oversampled simulation data with the addition of a Butterworth filter.

the limitation stated in Eq. (34). The order of the filter is flexible so long as the high-frequency noise is sufficiently suppressed. Achieving 10 dB attenuation at a spectral position located at about $1.1\kappa_{\zeta}^{\max}$ is usually acceptable.

Consider again the example with simulated data introduced in Section 4.1. In order to calculate α_{\max} in Eq. (33), we use the size of the region of interest, which is 30 cm by 30 cm by 3 cm, where the maximum range distance from the region of interest to the antenna is 6 cm. In addition, we use the shortest wavelength $\lambda_{\min} = 3.75$ cm. Then the maximum sampling step is obtained as $\Delta\zeta_{\max} \approx 1$ cm. This matches the maximum sampling step used in the simulation; thus, the final reconstruction is successful as shown in Figure 4(a). To emulate a sampling step $\Delta\zeta = 0.5$ cm, which is twice smaller than the originally used one, we resample the already available dataset using MATLAB's resample function [44]. Note that the area of the pixel in each slice of the image is now four times smaller since $\Delta\zeta$ determines the cross-range dimension of the pixel. The image reconstructed with such resampled data

without filtering is shown in Figure 8(a). Cross-shaped and point-like artifacts appear and the smaller scattering objects are hidden. This is because, despite the relatively accurate simulation, the data still contains numerical “noise” associated with the finite simulation grid. The resampling procedure also involves interpolation which inevitably introduces errors. Such noise and errors are amplified by the DFT and especially by the inversion with (30). With the application of a fourth-order Butterworth filter (Figure 7(b)), the artifacts are removed and the small scattering objects become visible (Figure 8(b)).

5. COMPARISON OF THE BORN AND RYTOV APPROXIMATIONS IN QMH USING TISSUE EXPERIMENTS

It is important to analyze and compare how both BA- and RA-QMH perform in highly nonlinear tissue reconstruction. The work in [22] showed that RA-QMH was able to outperform BA-QMH in the measurement of a chicken wing embedded in a lossy medium. Both BA- and RA-QMH failed to estimate correctly the values of the complex tissue permittivity, but the RA-QMH images did identify the shape and location of the chicken wing tissues in the phantom. BA-QMH, on the other hand, completely failed. The inability to produce useful quantitative information and the failure of BA-QMH was attributed to the excessive permittivity contrast between the background medium and the chicken wing. In that experiment, the chicken wing was embedded in a layer of lard which, in its turn, was embedded in a breast-tissue mimicking phantom material. The permittivity contrast among all three object components (chicken wing, lard, phantom material) was sufficiently high to violate the constraints of both the Born and the Rytov approximations.

The experiment in this work reduces the contrast between the tissue phantom and the host medium, which makes the task of the Born and Rytov approximations easier. A 20 cm by 20 cm by 1 cm tissue mimicking absorber sheet with a relative permittivity $\epsilon_r \approx 10 - i3$ is selected for the background medium. A circular cutout of the absorber sheet is made, and a petri dish is placed in the cutout. A chicken wing is placed in the center of the petri dish. S -parameter transmission data are acquired across a frequency bandwidth from 3 GHz to 8 GHz at 0.1 GHz intervals. The complex permittivities of all



Figure 9. The OUT constructed from peanut butter and jam (PBJ), an absorber sheet, and a chicken wing. Note that the skin of the chicken wing has been pulled to the left side of the wing. There are also two bones inside the chicken wing that run down the center underneath the muscle tissue.

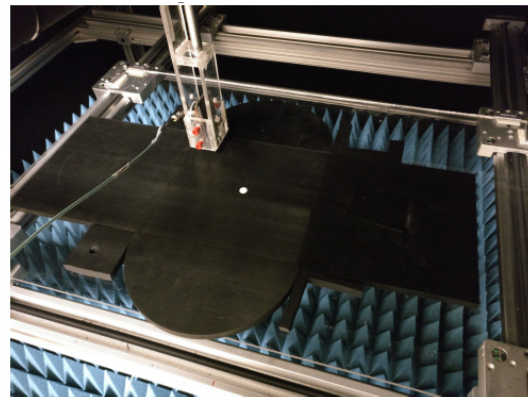


Figure 10. The CO phantom inside the acquisition setup. Two TEM horns, which are impedance matched to tissue, perform a raster scan across a 16 cm by 16 cm acquisition plane. The antennas are placed 2 mm above and below the tissue phantom. Extra absorbers are placed beside the phantom to reduce the impact of the air/absorber boundary at the edge of the phantom.

tissues and materials were measured with Agilent's coaxial probe [41] in this frequency band and were then averaged. The chicken wing is made up of muscle (measured average $\epsilon_r \approx 47.6 - i25.9$), skin (measured average $\epsilon_r \approx 14.4 - i6.2$), and bone (measured average $\epsilon_r \approx 21.5 - i10.7$). To remove the air gaps between the absorber sheet and the chicken wing, a host medium using peanut butter and jam (PBJ) is prepared. It is mixed in quantities of 40% peanut butter and 60% jam, with a measured average permittivity of $\epsilon_r \approx 7 - i3$. The PBJ is inserted around the chicken wing creating the OUT phantom as shown in Figure 9. The CO measurement is that of an absorber sheet with a small scattering probe (radius = 0.5 cm, height = 1 cm) of $\epsilon_r \approx 18 - i0$ inserted in the center, as shown in Figure 10. The RO is a solid absorber sheet with no insertions. Two TEM horn antennas [43], matched to tissue, are placed on either side of the RO, CO, and OUT phantoms. The antennas perform a raster scan with an output power of 0 dBm across a 16 cm by 16 cm acquisition plane at 0.2 cm intervals. The raw data of the RO and the CO are put through a denoising algorithm [42] to reduce the impact of measurement noise on the reconstruction.

The result of the RA-QMH reconstruction without apodization or low-pass filtering is shown in Figures 11(a) and 11(b). The images are noisy and no structures can be discerned. To improve the image quality, the apodization and post-inversion low-pass filters from Section 4 are applied. Figures 12(a) and 12(b) show the reconstruction with apodization filtering only. Speckling artifacts are visible

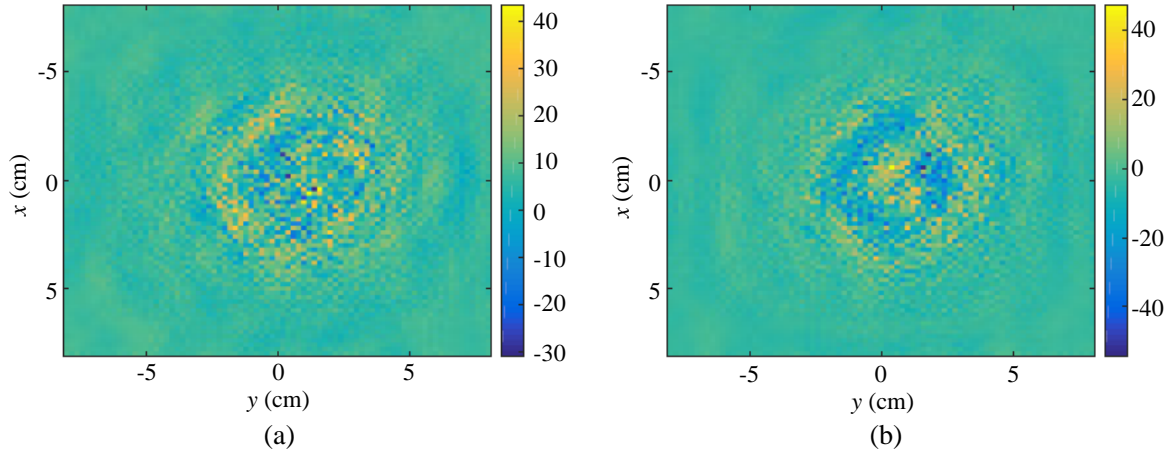


Figure 11. The RA-QMH reconstruction of the complex permittivity of the chicken wing without any filtering: (a) real part, (b) imaginary part. No structures can be discerned in both images.

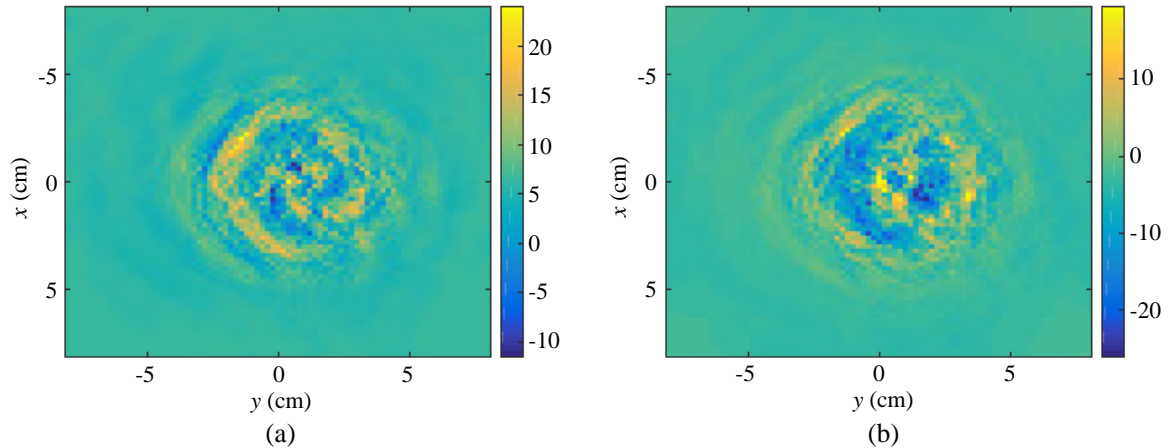


Figure 12. The RA-QMH reconstruction of the complex permittivity of the chicken wing with apodization filtering only: (a) real part, (b) imaginary part. No structures can be discerned in both images.

and large nonphysical permittivities exist in both the real and imaginary parts of the reconstruction. Figures 13(a) and 13(b) show the reconstruction with post-inversion low-pass filtering only. Here, the chicken wing and the background are not discernible in the image of the real part of the permittivity. When both filters are applied together, the reconstruction is improved as shown in Figures 14(a) and 14(b). The chicken wing is correctly localized within the ROI, and tissue structures such as skin and bone are partially visible in the reconstruction. For comparison, BA-QMH is also performed with the same filtering approaches, and the final images are shown in Figures 15(a) and 15(b).

There are similarities and differences between the BA-QMH and RA-QMH reconstructions aided by filtering and denoising. Firstly, they are both able to locate the chicken wing in the OUT. They also identify different tissue structures in the medium, such as the skin tissue on the left side of the chicken wing (high real part of the permittivity), and the bones that run down the middle of the chicken wing (near zero imaginary part of the permittivity). However, BA-QMH is also able identify the host PBJ medium and the absorber sheet interface. Further differences between the methods can be seen in their

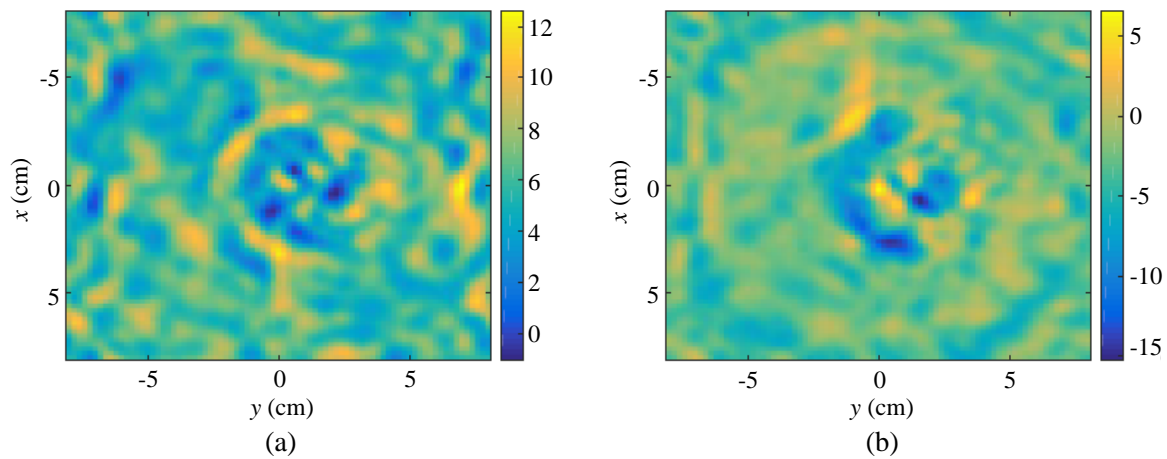


Figure 13. The RA-QMH reconstruction of the complex permittivity of the chicken wing with post-inversion low-pass filtering only: (a) real part, (b) imaginary part. No structures can be discerned in both images.

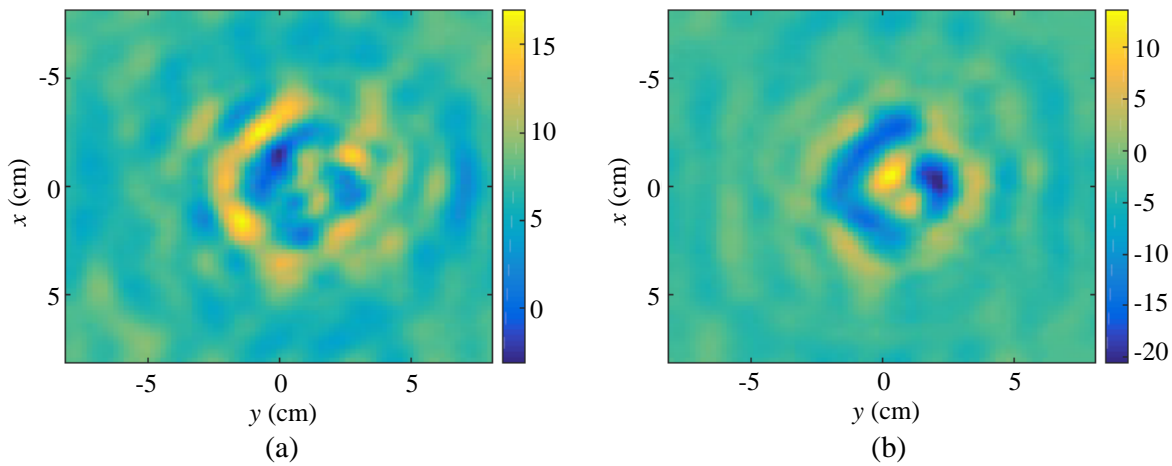


Figure 14. The RA-QMH reconstruction of the complex permittivity of the chicken wing with apodization and post-inversion low-pass filtering: (a) real part, (b) imaginary part. The chicken wing can be seen, and the skin is visible on the left side of the images. The bones are also partially visible. However, nonphysical values ($\text{Im}(\epsilon_r) > 0$) are observed.

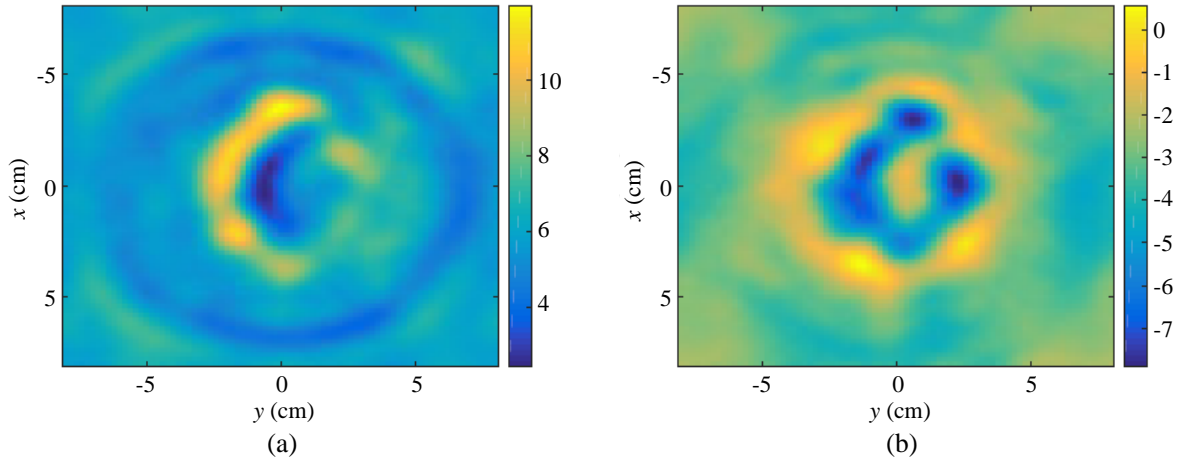


Figure 15. The BA-QMH reconstruction of the complex permittivity of the chicken wing with apodization and post-inversion low-pass filtering: (a) real part, (b) imaginary part. The chicken wing can be seen, and the skin in particular is visible on the left side of the images. The bones are seen in the imaginary part of the image.

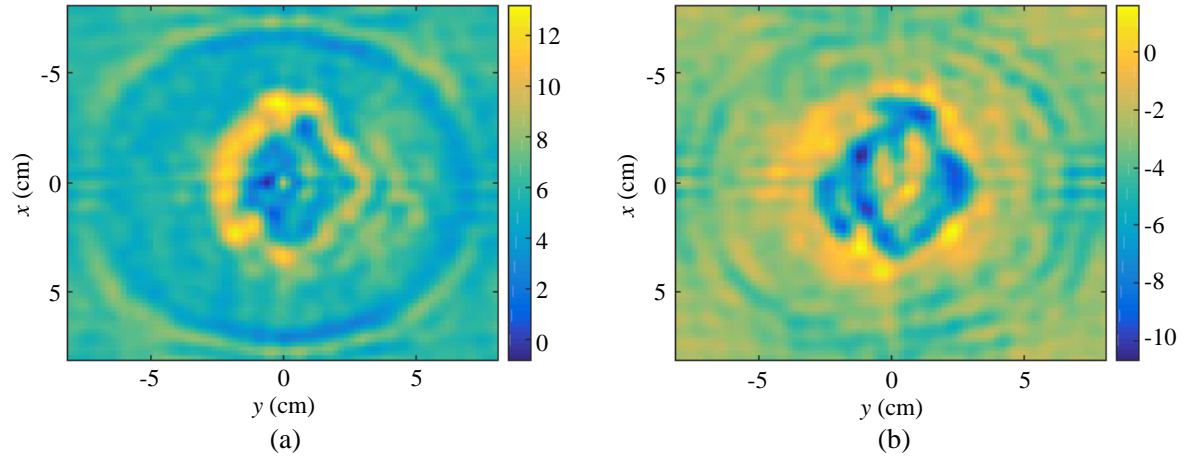


Figure 16. The BA-QMH reconstruction of the complex permittivity of the chicken wing with apodization and post-inversion low-pass filtering, but without denoising of the CO and RO datasets: (a) real part, (b) imaginary part. The resolution is improved compared to the images in Figures 15(a) and 15(b). The two separate bones are now visible in the imaginary part of the image.

quantitative outputs. The estimated permittivity values from the BA reconstruction are lower than the actual measured values. In comparison, the RA-based method produces slightly stronger quantitative values. But it also generates larger nonphysical permittivities, such as the positive imaginary responses in the center of the chicken wing (Figure 14(b)).

Contrary to the results shown in [22], BA-QMH appears to perform similarly to RA-QMH. This is due to the reduced contrast between the host medium (PBJ) and the chicken tissue on one hand, and between the host medium (PBJ) and the absorber sheet on the other. In the previous work, the chicken wing's individual tissue contrasts are negligible when compared to those with the background medium, making the wing appear electrically large and uniform. This violated the Born constraints, but did not impact the Rytov approximation significantly. Therefore, selecting a more appropriate host medium is critical to the performance of BA-QMH. It is also beneficial to RA-QMH.

It is interesting to consider the abilities of the two algorithms without denoising of the calibration

RO and CO datasets. In this comparison, only the filtering strategies discussed in Section 4 are applied. The RA-QMH strategy fails to produce an image, whereas BA-QMH generates a fairly clear image of the wing; see Figures 16(a) and 16(b). In fact, the BA-QMH image resolution with the non-denoised data is better than that with the denoised data. The two individual bones can be identified in the imaginary part of the reconstruction, and the edges of the wing are clearly defined. This is in fact an expected results since denoising often has an effect similar to low-pass filtering, leading to partial loss of resolution. We should also note that the phantom's relatively small thickness of 1 cm makes the task of BA-QMH easier. Born's approximation is constrained by Eq. (6), which depends on the length of the signal path through the OUT. Rytov's approximation gains no advantages from the thin phantom. Also, RA-QMH uses a logarithmic function to determine the scattered signal [see Eq. (8)], which may be more susceptible to noise than the subtraction used by BA-QMH.

From these experimental results, it is clear that tissue imaging presents a significant challenge to both RA-QMH and BA-QMH. Still, with the proper choice of the host medium, both BA- and RA-QMH are able to identify the tissue components. By using both approximations, complimentary reconstructions can be generated to verify and improve the overall linear reconstruction.

6. CONCLUSION

A quantitative microwave holography imaging method has been developed based on the linear Rytov model of scattering. Common artifacts created by QMH with both Rytov and Born's approximation are demonstrated and corrected using filters in a simulation example. An experimental example of a tissue measurement is shown, and both RA- and BA-QMH are used to reconstruct the complex permittivity of the tissue. The results demonstrate that in a tissue phantom designed to have an optimal host medium, BA-QMH performs similarly to RA-QMH, contrary to what was shown in previous work. In the case where no denoising strategy is applied, BA-QMH outperforms RA-QMH in terms of robustness to noise. The unique features of both reconstructions indicate a useful complementarity, which should be exploited in image analysis. Running both the RA-QMH and BA-QMH algorithms is possible due to their modest computational requirements. Both of them execute within a couple of seconds using MATLAB [44] on a 2013 Macbook Pro.

Future work aims at using either or both of the QMH implementations in an iterative method for the imaging of complex objects, such as human tissue. The utility of QMH in iterative imaging is two-fold. Firstly, QMH can provide the initial guess for the OUT complex permittivity distribution. This initial guess would be significantly better than the commonly used uniform background permittivity. Secondly, QMH can serve as the linear inversion module within each iteration of the nonlinear reconstruction. Before this can be done, however, the nonphysical values generated by the direct inversion method must be corrected either through customized filtering strategies or through the application of nonphysicality constraints in the solution of the inversion equations.

REFERENCES

1. Sheen, D. M., D. L. McMakin, and T. E. Hall, "Three-dimensional millimeter-wave imaging for concealed weapon detection," *IEEE Trans. Microwave Theory Tech.*, Vol. 49, No. 9, 1581–1592, Sep. 2001.
2. Xu, H., T. Li, and Y. Sun, "The application research of microwave imaging in nondestructive testing of concrete wall," *Proc. World Cong. Intell. Control Autom.*, 5157–5161, Dalian, 2006.
3. Kharkovsky, S. and R. Zoughi, "Microwave and millimeter wave nondestructive testing and evaluation — Overview and recent advances," *IEEE Instrum. Meas. Mag.*, Vol. 10, No. 2, 26–38, Apr. 2007.
4. Ahmad, F., M. G. Amin, and S. A. Kassam, "Synthetic aperture beamformer for imaging through a dielectric wall," *IEEE Trans. Aerosp. Electron. Syst.*, Vol. 41, No. 1, 271–283, Jan. 2005.
5. Amin, M. G., *Through-the-wall Radar Imaging*, CRC Press, 2016.
6. Nikolova, N. K., "Microwave biomedical imaging," *Wiley Encyc. Elec. Electron. Eng.*, 1–22, Apr. 25, 2014.

7. Conceio, R. C., J. J. Mohr, and M. O'Halloran, *An Introduction to Microwave Imaging for Breast Cancer Detection*, Springer, 2016.
8. Kwon, S. and S. Lee, "Recent advances in microwave imaging for breast cancer detection," *Int. J. Biomed. Imaging*, Vol. 2016, 25 pages, Article ID 5054912, 2016.
9. Bindu, G. N., S. J. Abraham, A. Lonappan, V. Thomas, C. K. Aanandan, and K. T. Mathew, "Active microwave imaging for breast cancer detection," *Progress In Electromagnetics Research*, Vol. 58, 149–169, 2006.
10. Porter, E., A. Santorelli, and M. Popovic, "Time-domain microwave radar applied to breast imaging: Measurement reliability in a clinical setting," *Progress In Electromagnetics Research*, Vol. 149, 119–132, 2014.
11. Wang, X., D. R. Bauer, R. Witte, and H. Xin, "Microwave-induced thermoacoustic imaging model for potential breast cancer detection," *IEEE Trans. Biomed. Eng.*, Vol. 59, No. 10, 2782–2791, Oct. 2012.
12. Xia, J., J. Yao, and L. H. V. Wang, "Photoacoustic tomography: Principles and advances (invited review)," *Progress In Electromagnetics Research*, Vol. 147, 1–22, 2014.
13. Fear, E. C. and M. A. Stuchly, "Confocal microwave imaging for breast tumor detection: A study of resolution and detection ability," *Proc. Int. Conf. IEEE Eng. Med. Bio. Soc.*, Vol. 3, 2355–2358, 2001.
14. Slaney, M., A. C. Kak, and L. E. Larsen, "Limitations of imaging with first-order diffraction tomography," *IEEE Trans. Microw. Theory Techn.*, Vol. 32, No. 8, 860–874, Aug. 1984.
15. Tu, S., J. J. McCombe, D. S. Shumakov, and N. K. Nikolova, "Fast quantitative microwave imaging with resolvent kernel extracted from measurements," *Inverse Probl.*, Vol. 31, No. 4, 045007 (33 pages), Apr. 2015.
16. Tricoles, G. and N. H. Farhat, "Microwave holography, applications and techniques," *Proc. IEEE*, Vol. 65, No. 1, 108–121, Jan. 1998.
17. Li, J., X. Wang, and T. Wang, "On the validity of Born approximation," *Progress In Electromagnetics Research*, Vol. 107, 219–237, 2010.
18. Habashy, T. M., R. W. Groom, and B. R. Spies, "Beyond the Born and Rytov approximations: A nonlinear approach to electromagnetic scattering," *J. Geophys. Res.*, Vol. 98, No. B2, 1759–1775, Feb. 1993.
19. Kak, A. and M. Slaney, *Principles of Computerized Tomographic Imaging*, Society for Industrial and Applied Mathematics, 2001.
20. Chew, W., *Waves and Fields in Inhomogeneous Media*, IEEE Press, 1995.
21. Nikolova, N. K., *Introduction to Microwave Imaging*, Cambridge University Press, 2017.
22. Tajik, D., D. S. Shumakov, and N. K. Nikolova, "An experimental comparison between the Born and Rytov approximations in microwave tissue imaging," *IEEE Int. Microw. Symp.*, Jun. 2017.
23. Farhat, N. H. and W. R. Guard, "Millimeter wave holographic imaging of concealed weapons," *Proc. IEEE*, Vol. 59, No. 9, 1383–1384, Sep. 1971.
24. Amineh, R. K., M. Ravan, J. McCombe, and N. K. Nikolova, "Three-dimensional microwave holographic imaging employing forward-scattered waves only," *Int. J. Antennas Propag.*, Vol. 2013, Article ID 897287 (15 pages), Feb. 2013.
25. Tajik, D., J. R. Thompson, A. S. Beaverstone, and N. K. Nikolova, "Real-time quantitative reconstruction based on microwave holography," *IEEE Int. Symp. Antennas Propag. (APS/URSI)*, 851–852, Fajardo, PR, 2016.
26. Amineh, R. K., J. J. McCombe, A. Khalatpour, and N. K. Nikolova, "Microwave holography using point-spread functions measured with calibration objects," *IEEE Trans. Instrum. Meas.*, Vol. 64, No. 2, 403–417, Feb. 2015.
27. Thompson, J. R., J. J. McCombe, S. Tu, and N. K. Nikolova, "Quantitative imaging of dielectric objects based on holographic reconstruction," *2015 IEEE Radar Conf. (RadarCon)*, 679–683, May 2015.
28. Khare, K., *Fourier Optics and Computational Imaging*, Wiley, 2016.

29. Mohamed, S. A., E. D. Mohamed, M. F. Elshikh, and M. A. Hassan, "Design of digital apodization technique for medical ultrasound imaging," *Int. Conf. Comput., Electr. Electron. Eng.*, 541–544, Khartoum, 2013.
30. Bell, R., "Introduction to Fourier transform spectroscopy," *Science*, 2012.
31. Beaverstone, A. S., D. S. Shumakov, and N. K. Nikolova, "Frequency-domain integral equations of scattering for complex scalar responses," *IEEE Trans. Microw. Theory Techn.*, Vol. 65, No. 4, 1120–1132, Apr. 2016.
32. Pastorino, M., *Microwave Imaging*, Wiley, 2010.
33. Natterer, F., "An error bound for the Born approximation," *Inverse Probl.*, Vol. 20, No. 2, 447–452, 2004.
34. Slaney, M., A. C. Kak, and L. E. Larsen, "Limitations of imaging with first-order diffraction tomography," *IEEE Trans. Microw. Theory Techn.*, Vol. 32, No. 8, 860–874, 1984.
35. Brown, M. A. and R. C. Semelka, *MRI: Basic Principles and Applications*, Wiley, 2015.
36. Anson, R. and M. Graves, *The Physics and Mathematics of MRI*, Morgan and Claypool, 2016.
37. Goodman, J. W., *Introduction to Fourier Optics*, Roberts and Company, 2005.
38. Szabo, T. L., *Diagnostic Ultrasound Imaging: Inside and Out*, Elsevier, 2014.
39. Jerri, A. J., *The Gibbs Phenomenon in Fourier Analysis, Splines, and Wavelet Approximations*, Springer-Science Business Media, B. V., New York, 2010.
40. EM Software & Systems — S. A. (Pty) Ltd., "FEKO Suite 7.0.1 for Altair," USA, 2016.
41. Keysight (Agilent) Technologies, "Dielectric Probe Kit 200 MHz to 50 GHz, 85070E," USA, 2014.
42. Shumakov, D. S., A. S. Beaverstone, and N. K. Nikolova, "De-noising algorithm for enhancing microwave imaging," *J. Eng.*, 5 pages, 2017.
43. Amineh, R. K., A. Trehan, and N. K. Nikolova, "TEM horn antenna for ultra-wide band microwave breast imaging," *Progress In Electromagnetics Research B*, Vol. 13, 59–74, 2009.
44. The MathWorks, Inc., "MATLAB 2016a," USA, 2016.